Effects of Thickness and Anisotropic Strain on Polarization Switching Properties of Sub-10 nm Epitaxial $Hf_{0.5}Zr_{0.5}O_2$ Thin Films

Kuan Liu(刘宽)[1], Kai Liu(刘楷)[1], Xingchang Zhang(张醒昌)[2], Jie Fang(方杰)[1], Feng Jin(金锋)[1], Wenbin Wu(吴文彬)[1,3], Chao Ma(马超)[2*], and Lingfei Wang(王凌飞)[1*]

[1]*Hefei National Research Center for Physical Sciences at the Microscale, University of Science and Technology of China, Hefei 230026, China*
[2]*College of Materials Science and Engineering, Hunan University, Changsha 410082, China*
[3]*Collaborative Innovation Center of Advanced Microstructures, Nanjing University, Nanjing 210093, China*

(Received 22 July 2024; accepted manuscript online 27 September 2024)

Doped HfO_2-based ferroelectric (FE) films are emerging as leading contenders for next-generation FE non-volatile memories due to their excellent compatibility with complementary metal oxide semiconductor processes and robust ferroelectricity at nanoscale dimensions. Despite the considerable attention paid to the FE properties of HfO_2-based films in recent years, enhancing their polarization switching speed remains a critical research challenge. We demonstrate the strong ferroelectricity of sub-10 nm $Hf_{0.5}Zr_{0.5}O_2$ (HZO) thin films and show that the polarization switching speed of these thin films can be significantly affected by HZO thickness and anisotropically strained $La_{0.67}Sr_{0.33}MO_3$-buffered layer. Our observations indicate that the HZO thin film thickness and anisotropically strained $La_{0.67}Sr_{0.33}MO_3$ layer influence the nucleation of reverse domains by altering the phase composition of the HZO thin film, thereby reducing the polarization switching time. Although the increase in HZO thickness and anisotropic compressive strain hinder the formation of the FE phase, they can enable faster switching. Our findings suggest that FE HZO ultrathin films with polar orthorhombic structures have broad application prospects in microelectronic devices. These insights into novel methods for increasing polarization switching speed are poised to advance the development of high-performance FE devices.

DOI: 10.1088/0256-307X/41/11/117701

Since the discovery in 2011,[1] HfO_2-based film ferroelectrics have attracted growing research interest due to their superior advantages in CMOS compatibility, scalability, and non-toxicity.[2,3] Recent studies have shown that the energy of the metastable ferroelectric (FE) phase in HfO_2-based films can be influenced by various factors, including ions doping,[4,5] top electrodes,[1,6,7] strain,[8,9] interface,[10,11] annealing temperatures,[12,13] and oxygen defects,[14,15] thus stabilizing multiple polarization states.[16,17] Utilizing the advent of HfO_2-based films, a variety of high-density FE non-volatile memory devices have been developed, including FE field effect transistors,[18,19] FE random access memories,[20,21] and FE tunnel junctions.[22,23] Considering that the data writing/reading processes in all these devices involve fast FE switching, understanding the domain configuration and switching characteristics of HfO_2-based FE systems is crucial for further optimizing these devices for practical applications.

Although the polarization switching time of HfO_2-based FeFETs can be reduced to below 1 ns using high pulse voltages,[19,24,25] the typical polarization switching time of HfO_2-based capacitors is approximately 1 μs.[26] Polarization-switching behaviors are strongly coupled with multiple parameters, including the non-FE phase, point defects, and grain size.[27,28] Several methods have been proposed to improve the switching speed of HfO_2-based films. For instance, post annealing at optimized temperatures and oxygen partial pressures can reduce the coercive field of doped polycrystalline HfO_2 films, leading to faster switching.[29,30] Increasing the volume fraction of non-FE phases or defects can lower the energy barrier for reverse domain nucleation, thereby reducing the switching time.[26,31–33] Increasing the thickness of HfO_2-based films increases the volume fraction of the non-FE phase, and the larger grain size is beneficial to the growth of FE domains, resulting in faster switching speed.[34,35] In addition, several research groups have utilized HfO_2 seed layers, composition gradient strategies, and HfO_2-ZrO_2 superlattice structures to achieve high polarization switching speed without degrading (even enhancing) the ferroelectricity of polycrystalline $Hf_{0.5}Zr_{0.5}O_2$ (HZO) films.[36–38]

In contrast to the polycrystalline HfO_2-based FE films with randomly oriented structural domains, epitaxial HZO films grown on perovskite-structure oxides [e.g. $La_{0.67}Sr_{0.33}MO_3$ (LSMO)] turn out to show uniform growth orientation. The considerably improved structural uniformity allows for effective control of ferroelectricity through a variety of tuning knobs, such as epitaxial strain,[39] film thickness,[40,41] interfacial structure,[10] and oxygen pressure.[42] Nevertheless, the polarization-switching dynamics of epitaxial HZO films have been

*Corresponding authors. Email: cma@hnu.edu.cn; wanglf@ustc.edu.cn
© 2024 Chinese Physical Society and IOP Publishing Ltd

rarely explored.

In this Letter, we delve into the significant impact of HZO thickness (t_{HZO}) and anisotropically strained LSMO layers on the polarization switching speed of HZO capacitors. Through systematic structural and electrical characterizations, we observe an enhancement of polarization switching speed by increasing t_{HZO} or imposing compressive anisotropic strain. Such a significant modulation of switching speed is highly related to the multi-phase domain configuration of HZO thin films. A higher proportion of the non-FE phase might reduce the energy barrier for reverse domain nucleation, thus increasing the switching speed. Our findings pave an effective tuning knob for controlling the switching speed of epitaxial FE HfO_2-based devices, providing valuable insights into the future optimization of FE device performance.

Method and Material. The LSMO/HZO/LSMO trilayer films were deposited by pulsed laser deposition method. The LSMO and HZO ceramic targets were prepared using the solid-state reaction method and ablated by a KrF excimer laser ($\lambda = 248\,\mathrm{nm}$). During film growing, the laser frequency and energy density were set at 5 Hz and $1.5\,\mathrm{J/cm^2}$, respectively. The substrate temperature was maintained at 700 ℃ for the LSMO layer and 900 ℃ for the HZO layer, under an oxygen partial pressure of 0.1 mbar. After deposition, the samples underwent *in situ* annealing for 15 min and then cooled to room temperature at a rate of 30 ℃/min.

X-ray diffraction (XRD) 2θ–ω linear scans and ω-scan rocking curves were conducted using a high-resolution x-ray diffractometer (PANalytical Empyrean) with Cu $K_{\alpha 1}$ radiation. Atomic-resolution high-angle annular dark-field (HAADF) scanning transmission electron microscopy (STEM) images were captured using a Thermo Scientific Titan Themis Z microscope operating at 300 kV and equipped with a probe-forming aberration corrector. A 30-nm-thick Pt layer was deposited on all HZO samples via DC magnetron sputtering at room temperature. Subsequently, an array of square-shaped Pt/LSMO electrode pads ($10 \times 10\,\mu\mathrm{m^2}$) was patterned using photolithography and ion milling. The polarization-electric field (P–E) hysteresis loops [both conventional and positive-up-negative-down (PUND) methods] of Pt/LSMO/HZO/LSMO capacitors were performed using a Radiant Precision Premier LC FE tester at 1 kHz. Non-FE factors can be excluded using the PUND method. Polarization switching measurements were performed using a Keithley 4200A SCS Semiconductor Parameter Analyzer.

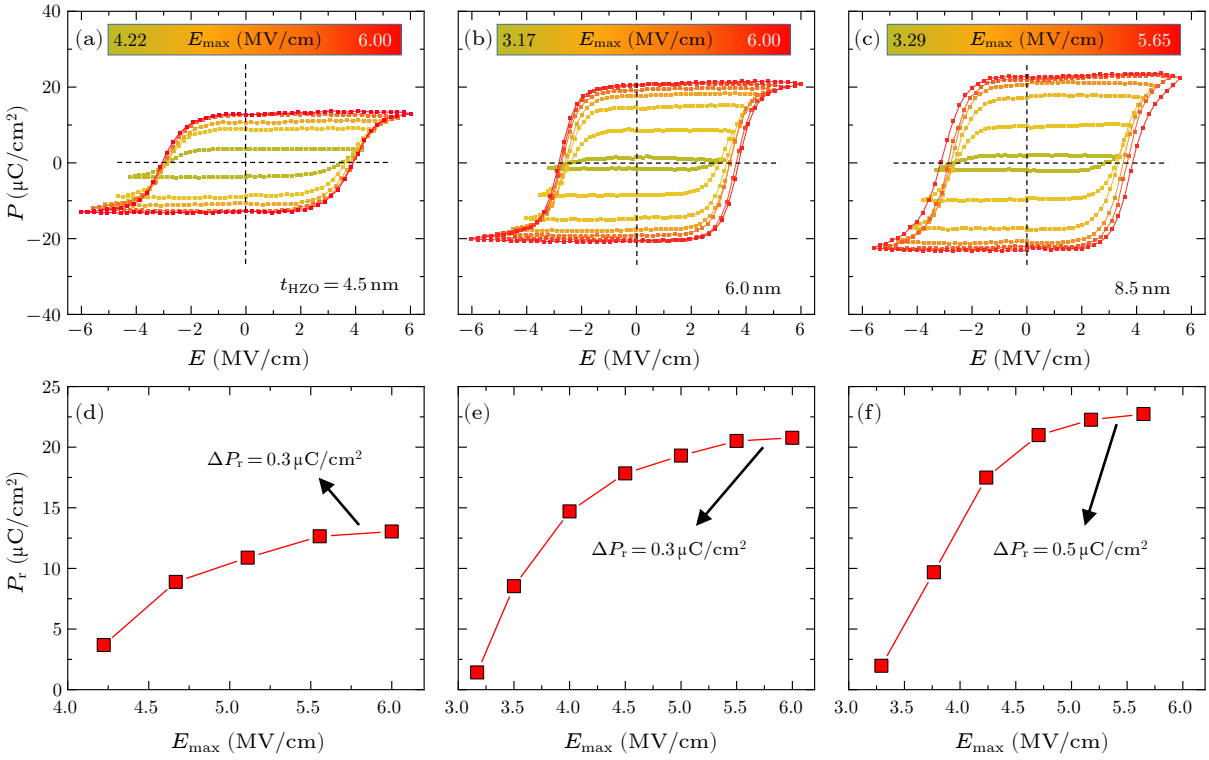

Fig. 1. Ferroelectric properties of Pt/LSMO/HZO/LSMO/STO(110) capacitors. (a)–(c) Polarization–electric field (P–E) hysteresis loops of Pt/LSMO/HZO/LSMO/STO(110) capacitors with various HZO layer thicknesses (t_{HZO}) = 4.5 (a), 6.0 (b), and 8.5 nm (c). These loops were obtained by the positive-up-negative-down (PUND) method. (d)–(f) Maximum $E(E_{\mathrm{max}})$-dependent remnant polarization (P_{r}) for LSMO/HZO/LSMO capacitor with $t_{\mathrm{HZO}} = 4.5$ (d), 6.0 (e) and 8.5 nm (f). A minimal ΔP_{r} indicates that the capacitors have reached saturation.

Results and Discussion. We first grew a series of LSMO/HZO/LSMO trilayer heterostructures on (110)-oriented $SrTiO_3$ [STO(110)] substrates. The thickness of LSMO layers was fixed at 20 nm, while the t_{HZO} was varied from 4.5 to 8.5 nm. XRD 2θ–ω linear scans exhibit distinct Laue fringes, indicating clear interfaces for all sam-

ples (Fig. S1 in the Supporting Information). The thickness measurements of the HZO and LSMO films, inferred from the Laue fringes, were consistent with the expected values based on the number of deposition pulses. XRD ω-scans and atomic force microscopy images further confirm the high epitaxial quality of the samples (Fig. S1). For instance, the sample with $t_{\rm HZO} = 4.5$ nm exhibits a small full width at half maximum of 0.036° and a surface root-mean-square roughness of 3.91 Å. The high epitaxial quality of these LSMO/HZO/LSMO/STO(110) trilayer heterostructures also results in robust ferroelectricity. To exclude the non-FE switching components from the P–E hysteresis loops, we utilized the PUND method to acquire the loops at room temperature under a bias frequency of 1 kHz (Fig. S2). Figures 1(a)–1(c) show the P–E hysteresis loops of LSMO/HZO/LSMO/STO(110) capacitors with $t_{\rm HZO} = 4.5$, 6.0, and 8.5 nm. All samples exhibit well-defined rectangular P–E hysteresis loops. As the maximum E ($E_{\rm max}$) increases, the P–E loops of all capacitors tend to saturate, indicating intrinsic FE behavior. Figure 1(d) shows the $E_{\rm max}$-dependent remnant polarization ($P_{\rm r}$) for the LSMO/HZO/LSMO capacitor with $t_{\rm HZO} = 4.5$ nm. As $E_{\rm max}$ increases from 5.56 to 6.00 MV/cm, $P_{\rm r}$ increases from 12.7 to 13.0 μC/cm^2, resulting in a $\Delta P_{\rm r}$ of only 0.3 μC/cm^2. This gives a saturation E ($E_{\rm s}$) of 5.56 MV/cm for the capacitor with $t_{\rm HZO} = 4.5$ nm. Similarly, according to Figs. 1(e) and 1(f), the capacitors with $t_{\rm HZO} = 6.0$ and 8.5 nm reach $E_{\rm s}$ of 5.50 and 5.18 MV/cm, respectively, with saturation polarization ($P_{\rm s}$) of 20.5 and 22.3 μC/cm^2. Notably, the capacitor with $t_{\rm HZO} = 8.5$ nm exhibits the largest $P_{\rm s}$ value. Researchers have shown that the volume fraction of the non-FE M phase is strongly correlated with the broad peaks in RCs.[5,43] We observed that the broad peaks in the RCs at HZO(111) becomes more pronounced with increasing $t_{\rm HZO}$ (Fig. S1), which may imply that the volume fraction of the non-FE M phase also increases. In addition, the dielectric constant for the capacitor with $t_{\rm HZO} = 4.5$ nm is 34.7 (Fig. S3), which is consistent with dielectric constant values reported for FE O phase ($Pca2_1$) HfO_2-based films.[44–46] As $t_{\rm HZO}$ increases, the dielectric constant slightly decreases (Fig. S3), which may be attributed to the increase in the volume fraction of the non-FE M phase, which has a lower dielectric constant.[47–49]

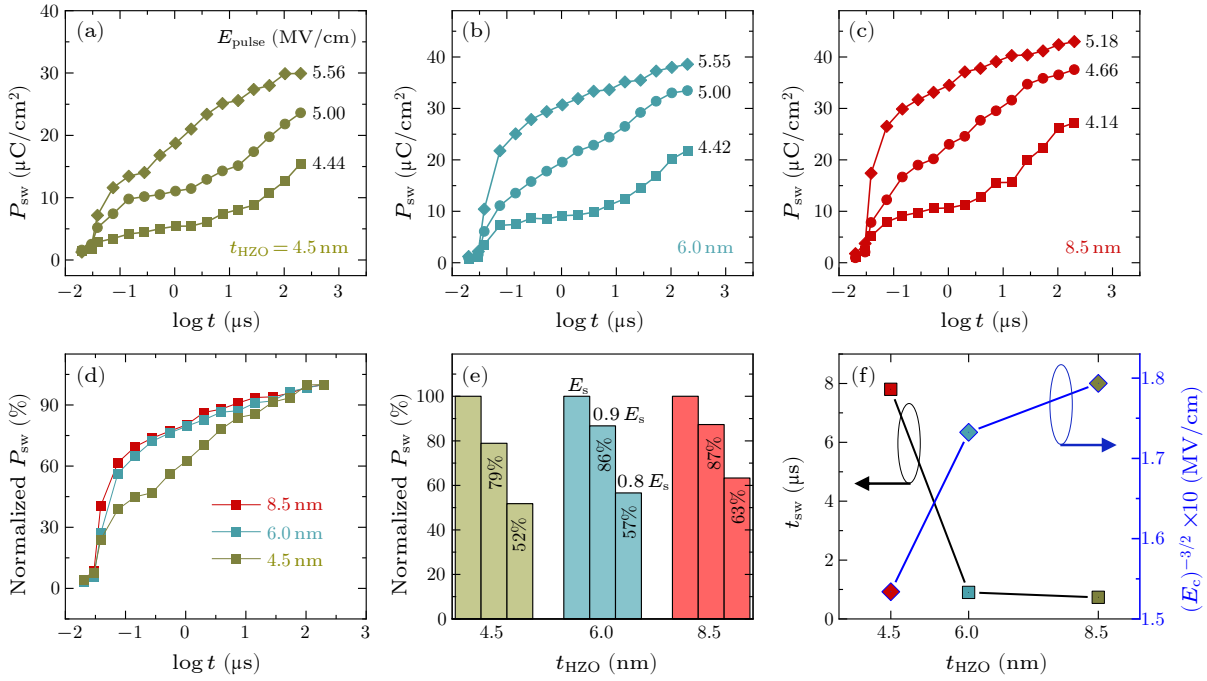

Fig. 2. Effect of $t_{\rm HZO}$ on the polarization switching speed of HZO capacitors. (a)–(c) Switched polarization ($P_{\rm sw}$) versus log t (t is pulse duration) for Pt/LSMO/HZO/LSMO/STO(110) capacitors with $t_{\rm HZO} = 4.5$ (a), 6.0 (b), and 8.5 nm (c). (d) Normalized $P_{\rm sw}$ versus log t for HZO capacitors with various $t_{\rm HZO}$ at a pulse amplitude equal to their respective saturation voltage. The normalized $P_{\rm sw}$ values were calculated by dividing the respective saturation $P_{\rm sw}$ values. (e) Normalized $P_{\rm sw}$ for three HZO capacitors at different $E_{\rm pulse}$ for $t = 200$ μs. (f) Variation of the polarization switching time ($t_{\rm sw}$) of the capacitors and $E_{\rm c}^{-3/2}$ values obtained from P–E hysteresis loop with $t_{\rm HZO}$.

We now quantitatively evaluate the switching speed of epitaxial HZO capacitors. As depicted in Fig. S4, we measured the switched polarization ($P_{\rm sw}$) of epitaxial LSMO/HZO/LSMO/STO(110) capacitors by adjusting the applied pulse duration (t) and amplitude. The electric field corresponding to the pulse voltage amplitude is recorded as $E_{\rm pulse}$. Figures 2(a)–2(c) depict the variation of $P_{\rm sw}$ with log t for capacitors with $t_{\rm HZO} = 4.5$, 6.0, and 8.5 nm, respectively. Higher $E_{\rm pulse}$ values cause larger $P_{\rm sw}$ values at earlier pulses. At the corresponding $E_{\rm pulse}$ of $E_{\rm s}$, the saturated $P_{\rm sw}$ increases with $t_{\rm HZO}$, aligning with the findings from the P–E loops (Fig. 1). Figure S5 displays the total current and non-FE switching current results for each capacitor under an $E_{\rm pulse}$ of $E_{\rm s}$. A decrease in leakage

current with increasing t_{HZO} may explain the reduced non-FE switching current. Figure 2(d) depicts the normalized P_{sw}–$\log t$ curves at E_s. The capacitor with $t_{HZO} = 8.5$ nm shows the highest normalized P_{sw} value at any given t, indicating that capacitors with larger t_{HZO} exhibit higher normalized P_{sw} under the same electrical conditions (E_s and t). Notably, even at an E_{pulse} of E_s, the capacitor with $t_{HZO} = 4.5$ nm experiences a gradual rather than rapid increase in normalized P_{sw} as t increases. Not only does the normalized P_{sw} increase with t_{HZO}, but the actual P_{sw} value does as well (Fig. S6). Figure 2(e) presents the normalized P_{sw} values of the three capacitors at $t = 200\,\mu$s under various E_{pulse} values. At an E_{pulse} of 0.8 E_s, only 52% of polarization switching occurs in the $t_{HZO} = 4.5$ nm capacitor, compared to 63% in the $t_{HZO} = 8.5$ nm capacitor. This indicates a positive correlation between t_{HZO} and the amount of polarization switching.

The switching speed of ferroelectrics is typically strongly correlated to the coercive field (E_c).[30] In FE films, the Kay–Dunn law describes the relationship between thickness (t_f) and E_c as $t_f = bE_c^{-3/2}$, where b is a constant.[50] However, the metastable nature of the FE phase in hafnium-based films,[51] complicates the observation of the Kay–Dunn law in these materials.[52] Polarization switching time (t_{sw}) is defined as the pulse duration required for a capacitor to achieve 80% polarization switching. Figure 2(f) illustrates the dependence of t_{sw} on t_{HZO} when capacitors with different t_{HZO} are subjected to a corresponding E_{pulse} of E_s. Figure 2(f) also shows the variation of $E_c^{-3/2}$ with t_{HZO} [the E_c values are obtained from Figs. 1(a)–1(c)]. While t_{HZO} is not directly proportional to $E_c^{-3/2}$, there is a strong correlation between t_{sw} and $E_c^{-3/2}$. A capacitor with $t_{HZO} = 10$ nm exhibits both the lowest E_c and shortest t_{sw}. Overall, as t_{HZO} increases, the stability of the non-FE phase increases, E_c decreases, and the polarization switching speed increases. The reduction in E_c could be attributed to the increased volume fraction of the non-FE phase.

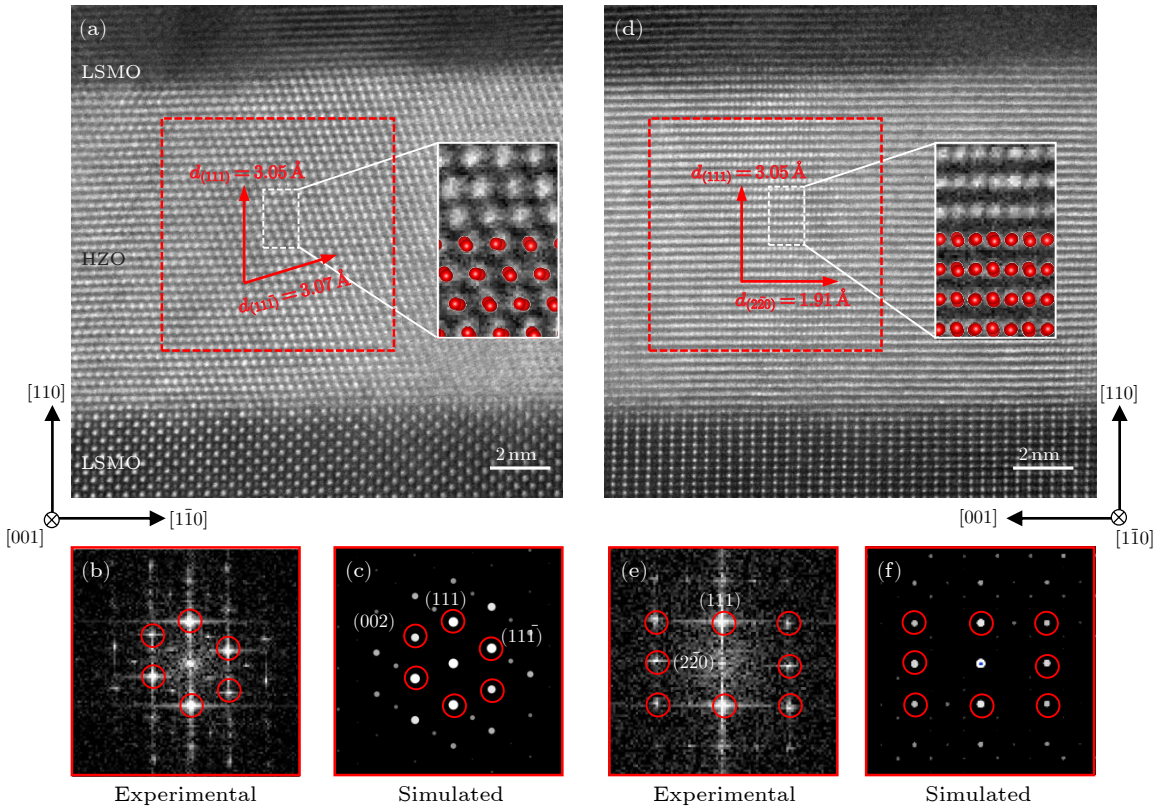

Fig. 3. Detailed examination of the microscopic polar structure in the HZO thin film. (a) Scanning transmission electron microscope (STEM) image along the STO[001] zone axis of the LSMO/HZO/LSMO/STO(110) sample, obtained using high-angle annular dark field (HAADF) mode. The inset shows the enlarged structure of the HZO thin film within the white dashed box, superimposed with the Hf atomic column projected along the [1$\bar{1}$0] zone axis of the orthorhombic (O) phase HfO_2. (b) Fast Fourier transform (FFT) diagram of the HZO section encased in the red box area within (a). (c) Simulated selected area electron diffraction (SAED) pattern of [111]-oriented O phase HfO_2 along the [1$\bar{1}$0] direction. The FFT and simulated SAED patterns share consistent intensity distributions. (d) HAADF-STEM image along the STO[1$\bar{1}$0] zone axis. The inset displays the enlarged structure of the HZO thin film within the white dotted box and a superposition of the Hf atomic column projected along the [$\bar{1}\bar{1}$2] zone axis of O phase HfO_2. (e) FFT diagram of HZO within the red box area in (d). (f) Simulated SAED pattern of [111]-oriented O phase HfO_2 along the [$\bar{1}\bar{1}$2] direction. The FFT and simulated SAED patterns exhibit nearly identical intensity distributions.

To determine the FE and non-FE domains of the LSMO/HZO/LSMO/STO(110) sample, we employed cross-sectional STEM characterizations. As shown in Fig. 3, we acquired STEM images in HAADF mode along two in-plane perpendicular zone axes: STO[001] and STO[1$\bar{1}$0]. The HAADF-STEM image along the STO[001] zone axis [Fig. 3(a)] displays two sets of atomic planes within the HZO layer, angled at 71° to each other, with similar interplanar spacings (3.05 Å and 3.07 Å). This atomic structure can be exclusively assigned to a (111)-oriented orthorhombic (O) domain, with the epitaxial relationship of HZO[1$\bar{1}$0]//STO[001]. Such a (111)-oriented O phase ($Pca2_1$) domain can be further verified by the fast Fourier transform (FFT) pattern [Fig. 3(b)] and simulated selected area electron diffraction (SAED) pattern [Fig. 3(c)]. The primary diffraction points, assigned by the same red circles as in Fig. 3(b), are indexed. The FFT and simulated SAED patterns share consistent intensity distributions, confirming the [111] out-of-plane orientation of HZO, with the [11$\bar{1}$] plane angled 71° from the out-of-plane orientation. Combined with the atomic structure comparison results, we conclude that Fig. 3(a) views the [1$\bar{1}$0] orientation of [111]-oriented O phase HZO.

Figure 3(d) presents the HAADF-STEM image observed along the STO[11$\bar{2}$] zone axis, indicating that HZO has an out-of-plane spacing of 3.05 Å and an in-plane spacing of 1.91 Å. This atomic structure can be specifically assigned to a (111)-oriented O domain with an epitaxial relationship of HZO[$\bar{1}\bar{1}$2]//STO[001]. The atomic structure comparison results, as well as the almost identical intensity distribution of the FFT pattern [Fig. 3(e)] and the SAED pattern [Fig. 3(f)], confirm that Fig. 3(d) corresponds to the [$\bar{1}\bar{1}$2] view of the [111]-oriented O phase HZO. Combining the HAADF-STEM findings from two perpendicular zone axes, we conclude that the polar phase of HZO in the LSMO/HZO/LSMO/STO(110) structure is definitively the O phase. Additionally, as shown in Figs. S7 and S8 in the Supporting Information, HAADF-STEM images along the two zone axes of STO[001] and STO[1$\bar{1}$0] confirm the coexistence of FE O and non-FE M phases in HZO thin films, the presence of low-crystalline regions between the O and M phase domains, and misaligned M phase domains. These observations support our hypothesis that the non-FE phase affects the broad peaks in the RCs, as well as the E_c and t_{sw}.

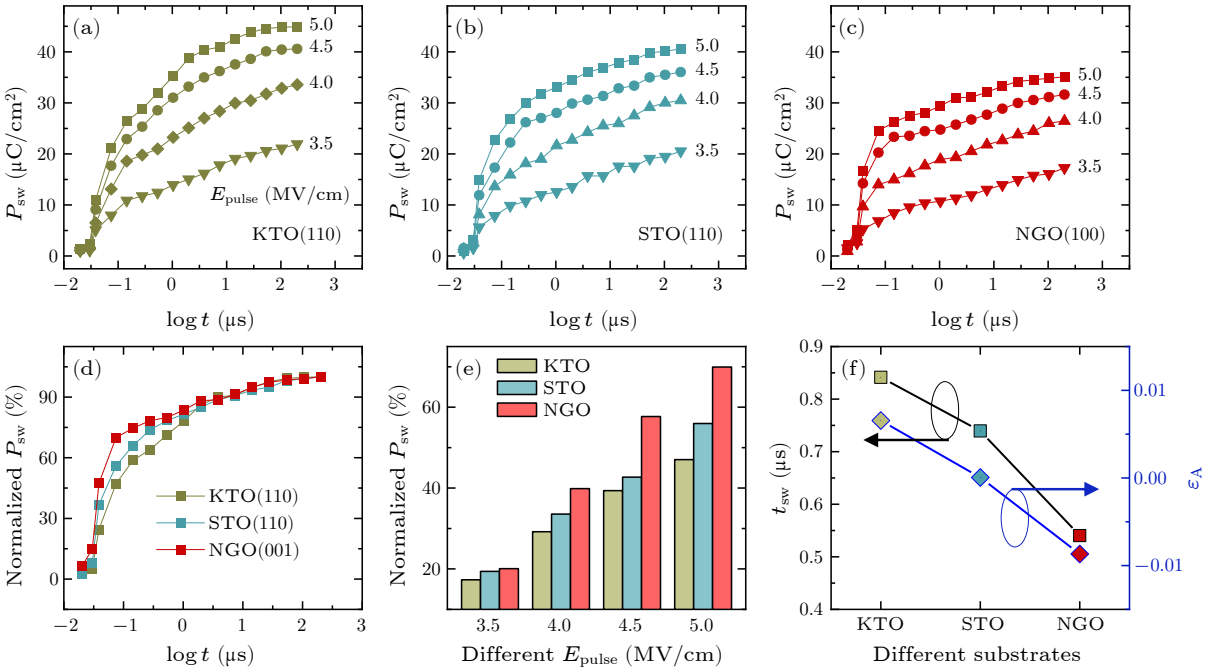

Fig. 4. Effect of anisotropic strain on the polarization switching speed of HZO capacitors. (a)–(c) P_{sw} versus log t for HZO capacitors epitaxially grown on KTO(110) (a), STO(110) (b), and NGO(001) (c) substrates. (d) Normalized P_{sw} versus log t for three HZO capacitors at E_{pulse} of 5 MV/cm. (e) Comparison of normalized P_{sw} for three HZO capacitors at t = 270 ns and different E_{pulse}. (f) Correlation between anisotropic strain values (ε_A) of the LSMO-buffered layer and t_{sw} for HZO capacitors on different substrates.

The nucleation-limited-switching (NLS) and Kolmogorov–Avrami–Ishibashi (KAI) models are two primary frameworks for understanding polarization switching dynamics in ferroelectrics.[53,54] The NLS model posits that the FE film consists of multiple independent polarization switching regions, with the nucleation time being the critical factor in determining the overall polarization switching speed. In contrast, the KAI model attributes the polarization switching speed primarily to the growth rate of FE domains. Notably, the polarization-switching behavior of our epitaxial HZO thin film adheres to the previously reported two-stage NLS model,[55] rather than the KAI model (Fig. S9). This observation enable us to speculate that an increased number of FE/non-FE interfaces

facilitates the initiation of nucleation in HZO thin films, thereby enhancing the polarization switching speed.[26] In addition, to date, we have not found any literature that reports the existence of "two stages" in the NLS model for polycrystalline HfO_2-based FE thin films, although a similar phenomenon has been observed in antiferroelectric $Hf_{0.4}Zr_{0.6}O_2$ thin films.[56] The mechanisms of "two stages" within the NLS model, as well as the specific impact of the non-FE phase on each stage, warrant further investigation in future studies.

To validate the influence of the non-FE phase on the polarization switching of HZO capacitors, we investigated the evolution of switching speed for three HZO capacitors grown on various substrates. According to our previous work, the volume fraction of the non-FE phase in epitaxial HZO thin films increases with the anisotropic compressive strain imposed on the bottom LSMO(110) electrodes.[57] Namely, the HZO thin films grown on LSMO-buffered NGO(100), STO(110), and KTO(110) are expected to show a gradually reduced proportion of non-FE phase. As shown in Figs. 4(a)–4(c), we characterized the P_{sw}–$\log t$ curves at various E_{pulse} values for LSMO/HZO/LSMO capacitors grown on KTO(110), STO(110), and NGO(100). Similar to the trend observed in Fig. 2, higher E_{pulse} results in higher P_{sw}. Figure 4(d) depicts the normalized P_{sw}–$\log t$ curves at an E_{pulse} of 5 MV/cm. The HZO capacitor grown on NGO(001) exhibits the highest normalized P_{sw} for t ranging from 20 ns to 2 µs, with no significant differences for t ranging from 2 µs to 200 µs. As shown in Fig. 4(e), we compared the amount of P_{sw} switched by HZO capacitors on various substrates at different E_{pulse} values at $t = 270$ ns. The HZO capacitor grown on NGO(001) achieves the largest fraction of polarization under the same conditions. Moreover, according to Fig. 4(f), the capacitor grown on KTO(110) needs the longest t_{sw} (0.84 µs), while the capacitor grown on NGO(001) needs the shortest t_{sw} (0.54 µs). The t_{sw} shows a strong correlation with the anisotropic strain ε_A imposed to the LSMO-buffered layers. A positive (negative) ε_A value indicates anisotropic tensile (compressive) strain along the in-plane $[1\bar{1}0]$ axis. Specifically, although anisotropic compressive strain does not favor the stability of the polar phase in epitaxial HZO, it does enhance the polarization switching speed. Additionally, the P_{sw} of the HZO capacitor grown on KTO(110) also adheres to the two-stage nucleation switching model (Fig. S10). Combined with the control of t_{HZO} and anisotropic strain on the switching speed, we propose that the increased FE/non-FE interfaces, resulting from the relatively higher volume fraction of the non-FE phase, are beneficial to the distributed nucleation of reverse domains, thus facilitating the polarization switching speed of our epitaxial HZO thin films (Fig. S11).

In summary, we have systematically investigated the impact of t_{HZO} and anisotropic strain on the FE switching speed of epitaxial HZO/LSMO heterostructures. The ε_r–E curves, XRD 2θ–ω linear scans, RCs, STEM images and E_c values indicate that the HZO thin films are mainly composed of the FE O phase, with the volume fraction of the non-FE M phase increasing as t_{HZO} increases from 4.5 to 8.5 nm. We therefore attribute the increase in P_r to the decrease in the depolarization field. At the same time, we observe a more than tenfold increment of polarization switching speed (t_{sw} decreases from 7.8 to 0.73 µs) by increasing t_{HZO} from 4.5 to 8.5 nm. Furthermore, we find that the anisotropic strain imposed on the LSMO bottom electrode can also modulate the proportion of the non-FE phase and thus the FE switching speed: as ε_A increases from −0.87% to 0.65%, t_{sw} decreases from 0.84 to 0.54 µs. The faster FE switching can be attributed to the favorable effect of the increase in the volume fraction of the non-FE M phase on the distributed nucleation of the reverse domains. Our findings underscore the significant effect of t_{HZO} and anisotropic strain states as effective tuning knobs on the FE switching speed of epitaxial HZO heterostructures, which may shed some light on the future developments of hafnium-based high-speed FE devices.

Acknowledgements. This work was supported by the National Key Research and Development Program of China (Grant Nos. 2023YFA1406404 and 2020YFA0309100), the National Natural Science Foundation of China (Grant Nos. 12074365, 12374094, 12304153, U2032218, and 11974326), CAS Project for Young Scientists in Basic Research (Grant No. YSBR-084), the Fundamental Research Funds for the Central Universities (Grant Nos. WK9990000102 and WK2030000035), Anhui Provincial Natural Science Foundation (Grant No. 2308085MA15), Hefei Science Center CAS Foundation (Grant Nos. 2021HSC-CIP017 and 2016HSC-IU06), the National Natural Science Foundation of China (Grant No. 12274120), the China Postdoctoral Science Foundation (Grant No. 2022M713060). The sample fabrication was partially carried out at the USTC Center for Micro and Nanoscale Research and Fabrication. All the authors appreciate the invaluable discussions and comments from Professor Shi Liu and Professor Mingmin Yang.

References

[1] Böscke T S, Müller J, Bräuhaus D, Schröder U, and Böttger U 2011 *Appl. Phys. Lett.* **99** 102903
[2] Schroeder U, Park M H, Mikolajick T, and Hwang C S 2022 *Nat. Rev. Mater.* **7** 653
[3] Banerjee W, Kashir A, and Kamba S 2022 *Small* **18** 2107575
[4] Martin D, Müller J, Schenk T, Arruda T M, Kumar A, Strelcov E, Yurchuk E, Müller S, Pohl D, Schröder U, Kalinin S V, and Mikolajick T 2014 *Adv. Mater.* **26** 8198
[5] Yun Y, Buragohain P, Li M, Ahmadi Z, Zhang Y, Li X, Wang H, Li J, Lu P, Tao L, Wang H, Shield J E, Tsymbal E Y, Gruverman A, and Xu X 2022 *Nat. Mater.* **21** 903
[6] Kim S J, Mohan J, Kim H S, Hwang S M, Kim N, Jung Y C, Sahota A, Kim K, Yu H Y, Cha P R, Young C D, Choi R, Ahn J, and Kim J 2020 *Materials* **13** 2968
[7] Wang X, Wen Y, Wu M, Cui B, Wu Y S, Li Y, Li X, Ye S, Ren P, Ji Z G, Lu H L, Wang R, Zhang D W, and Huang R 2023 *ACS Appl. Mater. Interfaces* **15** 15657
[8] Wei Y F, Nukala P, Salverda M, Matzen S, Zhao H J, Momand J, Everhardt A S, Agnus G, Blake G R, Lecoeur P, Kooi B J, Íñiguez J, Dkhil B, and Noheda B 2018 *Nat. Mater.* **17** 1095
[9] Liu S and Hanrahan B M 2019 *Phys. Rev. Mater.* **3** 054404

[10] Shi S, Xi H, Cao T, Lin W, Liu Z, Niu J, Lan D, Zhou C, Cao J, Su H, Zhao T, Yang P, Zhu Y, Yan X, Tsymbal E Y, Tian H, and Chen J 2023 *Nat. Commun.* **14** 1780
[11] Huang F, Saini B, Yu Z, Yoo C, Thampy V, He X, Baniecki J D, Tsai W, Meng A C, McIntyre P C, and Wong S 2023 *ACS Appl. Mater. Interfaces* **15** 50246
[12] Schroeder U, Mittmann T, Materano M, Lomenzo P D, Edgington P, Lee Y H, Alotaibi M, West A R, Mikolajick T, Kersch A, and Jones J L 2022 *Adv. Electron. Mater.* **8** 2200265
[13] Jang C H, Kim H S, Kim H, and Cha H Y 2022 *Materials* **15** 2097
[14] Ma L Y and Liu S 2023 *Phys. Rev. Lett.* **130** 096801
[15] Kaiser N, Song Y J, Vogel T, Piros E, Kim T, Schreyer P, Petzold S, Valentí R, and Alff L 2023 *ACS Appl. Electron. Mater.* **5** 754
[16] Mulaosmanovic H, Ocker J, Müller S, Schroeder U, Müller J, Polakowski P, Flachowsky S, van Bentum R, Mikolajick T, and Slesazeck S 2017 *ACS Appl. Mater. Interfaces* **9** 3792
[17] Jeon Y R, Kim D, Ku B, Chung C, and Choi C 2023 *ACS Appl. Mater. Interfaces* **15** 57359
[18] Kim S H, Yu G T, Park G H, Lee D H, Park J Y, Yang K, Lee E B, Lee J I, and Park M H 2021 *Chem. Commun.* **57** 12452
[19] Dahan M M, Mulaosmanovic H, Levit O, Dünkel S, Beyer S, and Yalon E 2023 *Nano Lett.* **23** 1395
[20] Henry M D, Smith S W, Fields S S, Jaszewski S T, Esteves G, Heinrich H, and Ihlefeld J F 2024 *IEEE Trans. Ultrason. Ferroelect. Freq. Control.* **71** 323
[21] Liao J, Dai S, Peng R C, Yang J, Zeng B, Liao M, and Zhou Y 2023 *Fundam. Res.* **3** 332
[22] Xu K, Wang T, Liu Y, Yu J, Li Z, Meng J, Zhu H, Sun Q, Zhang D W, and Chen L 2024 *ACS Appl. Electron. Mater.* **6** 1055
[23] Park J Y, Choe D H, Lee D H, Yu G T, Yang K, Kim S H, Park G H, Nam S G, Lee H J, Jo S, Kuh B J, Ha D, Kim Y, Heo J, and Park M H 2023 *Adv. Mater.* **35** 2204904
[24] Bae H, Nam S G, Moon T, Lee Y, Jo S, Choe D H, Kim S, Lee K H, and Heo J 2020 *IEEE International Electron Devices Meeting*, 12–18 December 2020, San Francisco, CA, USA, pp 31.3.1–31.3.4
[25] Chung W, Si M, Shrestha P R, Campbell J P, Cheung K P, and Peide D Y 2018 *IEEE Symposium on VLSI Technology*, 18–22 June 2018, Honolulu, HI, USA, pp 89–90
[26] Song T, Sánchez F, and Fina I 2022 *APL Mater.* **10** 031108
[27] Lee T Y, Lee K, Lim H H, Song M S, Yang S M, Yoo H K, Suh D I, Zhu Z, Yoon A, MacDonald M R, Lei X, Jeong H Y, Lee D, Park K, Park J, and Chae S C 2019 *ACS Appl. Mater. Interfaces* **11** 3142
[28] Chun M C, Park S, Park S, Park G Y, Kim M J, Cho Y, and Kang B S 2020 *J. Alloys Compd.* **823** 153777
[29] Yoo H K, Kim J S, Zhu Z, Choi Y S, Yoon A, MacDonald M R, Lei X, Lee T Y, Lee D, Chae S C, Park J, Hernker D, Langan J G, Nishi Y, and Hong S J 2017 *IEEE International Electron Devices Meeting*, 2–6 December 2017, San Francisco, CA, USA, pp 19.6.1–19.6.4
[30] Buyantogtokh B, Gaddam V, and Jeon S 2021 *J. Appl. Phys.* **129** 244106
[31] Li Y, Li J, Liang R, Zhao R, Xiong B, Liu H, Tian H, Yang Y, and Ren T L 2019 *Appl. Phys. Lett.* **114** 142902
[32] Lee K, Park K, Lee H J, Song M S, Lee K C, Namkung J, Lee J H, Park J, and Chae S C 2021 *Sci. Rep.* **11** 6290
[33] Lee D H, Yu G T, Park J Y, Kim S H, Yang K, Park G H, Ryu J J, Lee J I, Kim G H, and Park M H 2022 *Acta Mater.* **222** 117405
[34] Choi S N, Moon S E, and Yoon S M 2019 *Ceram. Int.* **45** 22642
[35] Sawabe Y, Saraya T, Hiramoto T, Su C J, Hu V P H, and Kobayashi M 2022 *Appl. Phys. Lett.* **121** 082903
[36] Liu C, Yang Q, Zeng B, Jiang Y, Zheng S, Liao J, Dai S, Zhong X, Zhou Y, and Liao M 2022 *Adv. Funct. Mater.* **32** 2209604
[37] Hao P, Zheng S, Zeng B, Yu T, Yang Z, Liao L, Peng Q, Yang Q, Zhou Y, and Liao M 2023 *Adv. Funct. Mater.* **33** 2301746
[38] Kang M, Peng Y, Xiao W, Zhang Y, Wang Z, Du P, Jiang H, Liu F, Liu Y, Hao Y, and Han G 2024 *ACS Appl. Mater. Interfaces* **16** 2954
[39] Estandía S, Dix N, Gazquez J, Fina I, Lyu J, Chisholm M F, Fontcuberta J, and Sánchez F 2019 *ACS Appl. Electron. Mater.* **1** 1449
[40] Song T F, Bachelet R, Saint-Girons G, Dix N, Fina I, and Sánchez F 2021 *J. Mater. Chem. C* **9** 12224
[41] Gao R, Liu C, Shi B, Li Y, Luo B, Chen R, Ouyang W, Gao H, Hu S, Wang Y, Li D, and Ren W 2024 *Chin. Phys. Lett.* **41** 087701
[42] Lyu J, Fina I, Solanas R, Fontcuberta J, and Sánchez F 2019 *ACS Appl. Electron. Mater.* **1** 220
[43] Zhou C, Ma L, Feng Y, Kuo C Y, Ku Y C, Liu C E, Cheng X, Li J, Si Y, Huang H, Huang Y, Zhao H, Chang C F, Das S, Liu S, and Chen Z 2024 *Nat. Commun.* **15** 2893
[44] Sang X, Grimley E D, Schenk T, Schroeder U, and LeBeau J M 2015 *Appl. Phys. Lett.* **106** 162905
[45] Wang Y, Wang Q, Zhao J, Niermann T, Liu Y, Dai L, Zheng K, Sun Y, Zhang Y, Schwarzkopf J, Schroeder T, Jiang Z, Ren W, and Niu G 2022 *Appl. Mater. Today* **29** 101587
[46] Chen W C, Zhang Y C, Chen P H *et al.* 2020 *J. Phys. D* **53** 445110
[47] Lin Y S, Puthenkovilakam R, and Chang J P 2002 *Appl. Phys. Lett.* **81** 2041
[48] Tan T T, Liu Z T, and Li Y Y 2011 *Chin. Phys. Lett.* **28** 086803
[49] Yang L 2010 *Chin. Phys. Lett.* **27** 077102
[50] Kay H F and Dunn J W 1962 *Philos. Mag.* **7** 2027
[51] Batra R, Tran H D, and Ramprasad R 2016 *Appl. Phys. Lett.* **108** 172902
[52] Tasneem N, Yousry Y M, Tian M K, Dopita M, Reyes-Lillo S E, Kacher J, Bassiri-Gharb N, and Khan A I 2021 *Adv. Electron. Mater.* **7** 2100485
[53] Tagantsev A K, Stolichnov I, Setter N, Cross J S, and Tsukada M 2002 *Phys. Rev. B* **66** 214109
[54] Shur V, Rumyantsev E, and Makarov S 1998 *J. Appl. Phys.* **84** 445
[55] Wei Y, Vats G, and Noheda B 2022 *Neuromorph. Comput. Eng.* **2** 044007
[56] Park M H, Kim H J, Lee Y H, Kim Y J, Moon T, Kim K D, Hyun S D, and Hwang C S 2016 *Nanoscale* **8** 13898
[57] Liu K, Jin F, Zhang X, Liu K, Zhang Z, Hua E, Zhang J, Ye H, Gao G, Ma C, Wang L, and Wu W 2023 *Adv. Funct. Mater.* **33** 2209925